CrossMark

Fabrication of Ni–P coating film on diamond/Al composite and its soldering reliability

Qi-Yuan Shi[1,2] · Zhi-Quan Liu[1,2,3] · Di Wu[1] · Hao Zhang[3] · Ding-Rui Ni[1] · Katsuaki Suganuma[3]

Abstract
Although the diamond/Al composite is a good heat sink material due to its high thermal conductivity and low cost, its surface cannot be wetted directly for microelectronic packaging. Using modified electroless plating procedures and recipes, a glossy, continuous, and uniform Ni–P film was successfully fabricated on the diamond/Al composite surface for the first time with a bonding strength of 15.1 MPa. This Ni–P coating layer is solderable for both lead-free SAC305 and Sn63Pb37 alloys on Cu dummy chips. A continuous intermetallic compound (IMC) layer was formed at the interface without any crack or void defects, and the shear strength of both solder joints was in the range of 39.9–41.2 MPa. During thermal storage tests, the growth of IMC was slow at 125 and 150 °C, but it elevated sharply at 175 °C. According to growth kinetics analyses, a Ni element can hinder IMC growth. The diffusion activation energy (Q) of $(Cu,Ni)_6Sn_5$ was calculated as 62.6 kJ/mol in SAC305 and 97.7 kJ/mol in Sn63Pb37 solder joints. Both microstructures and mechanical properties of the solder joint using the Ni–P coated diamond/Al composite can satisfy the requirement of microelectronic industrial applications.

1 Introduction

When power electronic devices and circuits work, they inevitably produce heat. Heat accumulation leads to the rise of temperature, thereby harming the devices. In addition, the traditional air cooling method has been unable to meet the high-density heat dissipation requirement. Hence, some thermal interfacial materials with peculiar properties were utilized in order to transmit the harmful heat to the air. These materials were called heat sink materials [1, 2]. As a type of heat dispersing material, heat sink materials must possess a low coefficient of thermal expansion and excellent thermal conductivity [3, 4]. Particularly, they have to also possess comparatively low density so as to be applied in the electronic industry. Diamond is a material with the

best temperature conductivity for this purpose. On the other hand, the appearance of artificial diamond leads to the constant decrease in its price. It appears to be a feasible way to improve the temperature conductivity of the metals, such as Al, Cu, and Ag, by embedding the diamond into them. By controlling the content of the diamond in the metal substrate, we can adjust its coefficient of thermal expansion to match that of the thermal expansion of Si, GaAs, etc. [5]. With respect to the density, the expense, and the temperature conductivity, Al is superior to the commonly used Al, Cu, and Ag substrate materials. The diamond/Al composite can be applied to some vital devices in the aerospace and military industry. Due to its tremendous potentialities in the electronic packaging industry, many researchers have managed to fabricate diamond/Al composites by various methods [5–8]. In addition, plenty of investigations on the enhancement of its properties have also been conducted [9–14].

However, due to the addition of diamond particles with poor wettability in Al substrates, diamond/Al composite is difficult to be wetted and, therefore, cannot be soldered directly with chips, which greatly limits the application of the composite. Therefore, it is vital to find an approach to enhance its solderability. Electroless plating is one of the methods that is widely used in surface metallization [15–17]. Compared with electroplating [18, 19], electroless plating requires fewer procedures and no electric source, which

✉ Zhi-Quan Liu
zqliu@imr.ac.cn; zhiquanliu@yahoo.com

✉ Hao Zhang
zhanghao@alum.imr.ac.cn

[1] Institute of Metal Research, Chinese Academy of Sciences, Shenyang 110016, China

[2] School of Materials Science and Engineering, University of Science and Technology of China, Shenyang 11016, China

[3] The Institute of Scientific and Industrial Research, Osaka University, Osaka 567-0047, Japan

eventually helps the producers save much cost. Through this process, therefore, a metal layer of uniform thickness and strong cohesion can be deposited on the composite surface through a redox reaction. Until now, many metals have been tested for diamond/metal electroless plating [20–22]. Among these metals, the nickel-phosphorus coating has been proved to be an optimized choice not only due to its good solderability and wide applications but also its simple process and cheap fabrication cost [23]. However, in addition to the many literatures on the coating of diamond/Cu composites, no systematic study has been performed on the fabrication of Ni–P coating on diamond/Al until now despite its solderability and reliability in the microelectronic industry.

In this work, electroless plating was used to successfully fabricate the Ni–P coating film on diamond/Al composite surface for the first time, which remarkably improved the solderability of the composite. A series of designed tests were conducted to analyze and estimate the reliability of coating and soldering structure systematically, which shed light on the potential applications of Ni–P coated diamond/Al composite in the microelectronic industry.

2 Experimental procedures

2.1 Sample preparation and electroless deposition

The diamond/Al composites were fabricated using the method of powder metallurgy, whose use has been reported elsewhere [13, 24]. The composites were processed into several cuboids whose size was 10 mm × 10 mm × 2 mm as substrate. The sample surface was first polished with boron carbide to preliminarily smoothen the surface as it is difficult to produce a coating on diamond/Al rough surface if little diamond particles are embedded in the Al substrate. The polished composites were then washed with deionized water and subjected to ultrasonic treatment in acetone for 2 min to clean the surface. Consequently, we rinsed the composites with deionized water several times and used 10 wt% H_2SO_4 to roughen the surface. To sensitize the surface, further washing was carried out with deionized water and a mixed solution containing 10 g/L $SnCl_2 \cdot H_2O$ with 10 mL/L HCl. After washing the composites with deionized water again, the samples were immersed in a mixture of 0.5 g/L $PdCl_2$ and 10 mL/L HCl for 1 min to activate the surface. Subsequently, the composites were rinsed again and then plated.

The components of electroless plating solutions are $NiSO_4 \cdot 6H_2O$, $NaH_2PO_2 \cdot H_2O$, $Na_3C_6H_5O_7$, $C_3H_6O_3$, NaAc,

and thiourea. Detailed concentrations of the components are shown in Table 1. The solution's pH was adjusted to 4.8. The electroless plating process was carried out in the water bath at 85 °C without a protective atmosphere. The plating time was varied from 30 to 215 min in order to obtain the growth curve of the Ni–P coating film. The thickness of the coating film that was used in this study was about 30–40 μm.

2.2 Soldering and high temperature storage

Both Sn63Pb37 and SAC305, a typical lead solder and a lead-free solder with outstanding characteristics, respectively, were testified on Ni–P coatings to form solder joints. The designed joint comprised a Cu dummy chip (3 mm × 3 mm × 0.2 mm), a solder plate (3 mm × 3 mm × 0.8 mm), and a composite substrate (10 mm × 10 mm × 2 mm). The soldering process was conducted at a temperature that was 20° higher than the melting points of SAC305 (217 °C) and Sn63Pb37 (183 °C) for 1 min and was followed by subjection to air cooling.

For service reliability study, solder joints were also stored in the thermal storage oven at three different temperatures (125, 150, and 175 °C) for different periods (7, 16, and 25 days). The interfacial evolution of the intermetallic compounds (IMCs) was characterized, and their diffusion coefficients at variable storage temperatures were calculated. Microstructural observations were carried out using a scanning electron microscope (SEM, Quanta 600, FEI, America) and while being equipped with an energy-dispersive spectroscopy (EDS), focusing on the surface morphology, interfacial reactions, as well as the defect formation therein.

2.3 Bonding and shear strength test

After electroless deposition, the interface bonding strength between the diamond/Al substrate and the Ni–P coating film was tested by an electronic tensile testing machine (Romulus III-A universal materials tester, Quad Group Inc., America), as shown in Fig. 1a. A stud with a diameter of 2.7 mm was vertically attached to the horizontal surface of the sample using a thin film of epoxy, which enabled testing the bond strength under 70 MPa at a loading rate of 1.5 N/s. After soldering, the shear strength of the solder joint was tested by the bond tester (DAGE4000, Nordson DAGE, Great Britain) whose detailed schematic diagram is shown in Fig. 1b. At least five samples were tested for each kind of solder joint. X-ray diffraction (XRD) test on Ni–P coating, which was aimed at investigating its phase structure, was conducted by

	$NiSO_4 \cdot 6H_2O$	$NaH_2PO_2 \cdot H_2O$	$Na_3C_6H_5O_7$	$C_3H_6O_3$	NaAc	Thiourea
Table 1 Recipe for electroless plating bath (unit g/L)	25	25	5	0.02	15	0.0035

Fig. 1 Schematic diagram of **a** bond strength test and **b** shear strength test
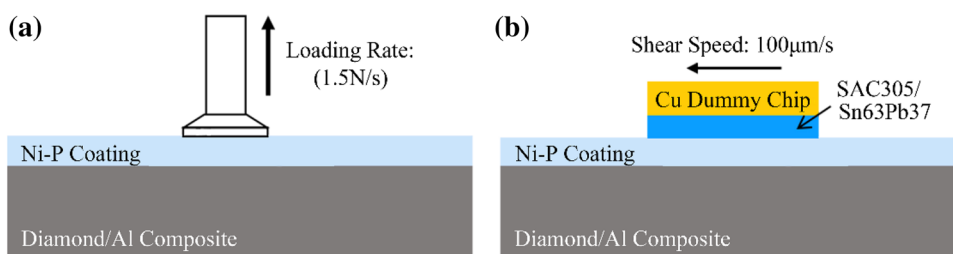
an X-ray diffractometer (Rigaku D/max-2400, Tokyo, Japan) with Cu Kα radiation (λ = 1.54178 Å) using scanning 2θ angle from 20° to 85°.

3 Results and discussion

3.1 Successful fabrication of Ni–P coating film

Before electroless deposition, the polished surface of the diamond/Al composite was extremely rough, as shown in Fig. 2a. Tiny diamond particles that are hard to be wetted were randomly distributed on the rugged surface of Al substrate, which implied a poor wettability of diamond/Al surface. After electroless deposition, as displayed in Fig. 2b,

the original rugged surface was totally covered by a coating layer, which, thereby, turned out to have a bubble-shaped morphology. The cross-sectional view of the coating film on the diamond/Al composite is shown in Fig. 2c. A continuous Ni–P film was deposited on the composite surface with a thickness of about 30–40 μm. Diamond particles were buried within the coating layer, and the film was uniform without any cracks or pores. Through EDS analysis, as shown in Fig. 2d, it was found that this coating layer mainly comprised Ni (92–94 at.%) and P (6–8 at.%) elements. The content of P was successfully controlled below 10 at.% and varied little. Figure 2 proves the successful fabrication of Ni–P coating on diamond/Al composite surface. The thickness of the coating film can ensure that it would meet the requirements of its application in the microelectronics industry
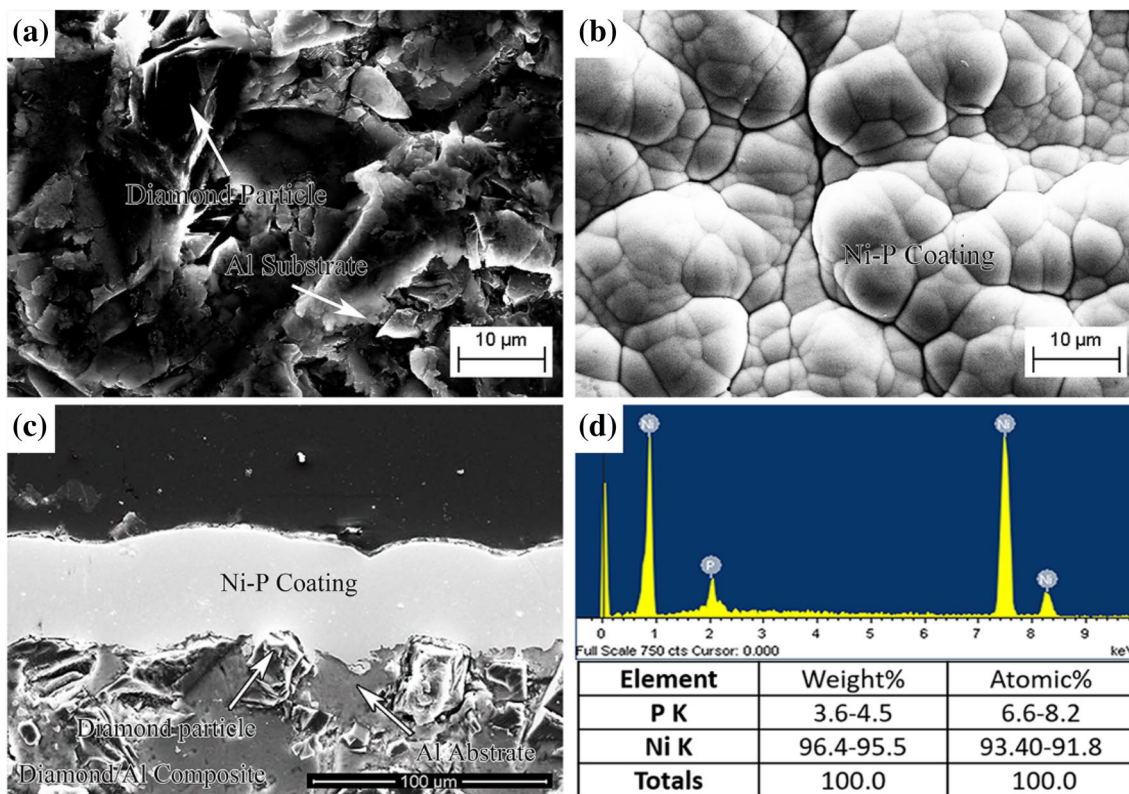

Element	Weight%	Atomic%
P K	3.6–4.5	6.6–8.2
Ni K	96.4–95.5	93.40–91.8
Totals	100.0	100.0

Fig. 2 Surface morphology of diamond/Al composite surfaces **a** before and **b** after electroless coating, **c** cross-sectional view of coated diamond/Al composite and **d** EDS analysis result of Ni–P coating

(MIL-C-26074, the minimum thickness of the nickel coating shall be 0.0010 in./0.0026 mm). This Ni–P coating film enables the excellent binding status on diamond/Al substrate, which ensures its steady and good performance hereafter.

The bonding strength between Al substrate and Ni–P coating was tested using ten samples, and the average bonding strength was measured to be about 15.1 MPa. The morphology of the fracture interface after the test is presented in Fig. 3. Up-right inset is an enlarged image of the cracked edge. It was clear that failure happened in the Ni–P film and the composite substrate but not in the Ni–P coating layer. This verified that the quality of electroless deposited in Ni–P coating layer was good enough, being homogeneous and uniform without any defects such as cracks and pores inside.

The successful fabrication of the Ni–P coating layer on the composite substrate was attributed not only to the plating solution's composition but also to the pretreatment process. As the surface of diamond particles is hydrophobic and could hardly be immersed in the solution for coating, the conduction of the sensitization and activation procedures of the diamond/Al composite surface was necessary before electroless deposition. During these processes, Sn^{2+} in the $SnCl_2$ sensitizing solution reacts with Pd^{2+} in the $PdCl_2$ activating solution to reduce the Pd^{2+} ions into Pd, which, afterward, acts as the catalytic center of the Ni–P coating deposition reaction. The reaction formula can be described as formula (1) [25]. During the electroless plating procedure, the mechanism of Ni–P deposition can be understood, considering the formulae from (2) to (4) [26] as follows:
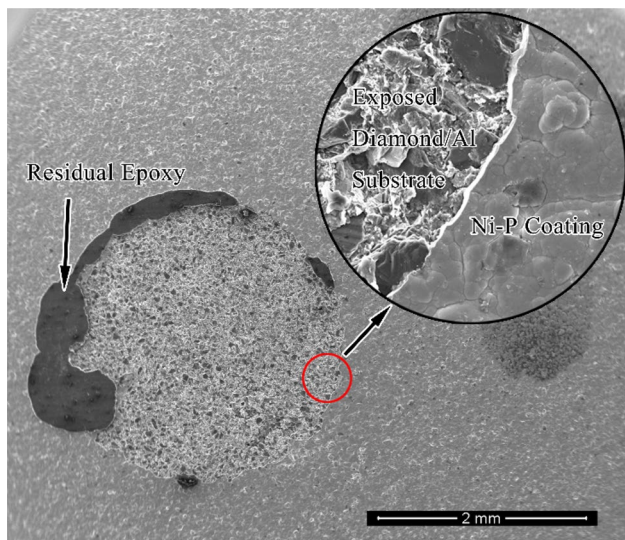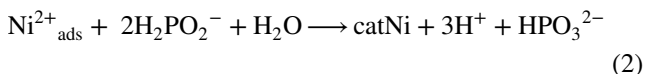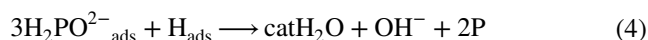
$$Pd^{2+} + Sn^{2+} \rightarrow Sn^{4+} + Pd \tag{1}$$

$$Ni^{2+}_{ads} + 2H_2PO_2^- + H_2O \longrightarrow catNi + 3H^+ + HPO_3^{2-} \tag{2}$$

$$H_2PO^{2-}_{ads} + H_2O \longrightarrow catHPO_3^{2-} + H_2 + 2H_{ads} \tag{3}$$

$$3H_2PO^{2-}_{ads} + H_{ads} \longrightarrow catH_2O + OH^- + 2P \tag{4}$$

It is clear that the deposition of Ni–P coating is a consequence of the redox reaction between the Ni^{2+} and H_2PO^{2-} ions. The concentration of H_2PO^{2-} in the bath has a vital effect on the phosphorus content in the Ni–P coating, which eventually determines the properties of the coating. With a higher content of phosphorus, the coating layer has better corrosion resistance, but rougher surface, lower binding force, and worse heat resistance [20]. Considering its application conditions, relevantly lower phosphorus content in Ni–P coating is more suitable, as shown in Fig. 2d. Meanwhile, in order to maintain a steady and durable electroless plating bath, complex agent, stabilizer, and buffering agent were added, and their concentrations were carefully controlled to optimize the quality of the coating and to reduce the cost.

In order to control the growth process of the coating layer, the thickness of Ni–P film as a function of plating time is shown in Fig. 4. When the plating time varies from 30 to 135 min, the relationship between the plating time and the film thickness is nearly linear before a 50 μm thickness is achieved. However, when the plating time is more than 135 min, the film growth rate decreases and the profile gradually declines. This phenomenon should result from changes in the bath components due to consumption. As the plating continues, more and more Ni^{2+} ions are consumed and its concentration decreases, which results in a decrease in the growth rate of the film. However, a 20 μm thickness with a plating time of less than 30 min is enough for normal applications as a under-bump metallization (UBM) film.
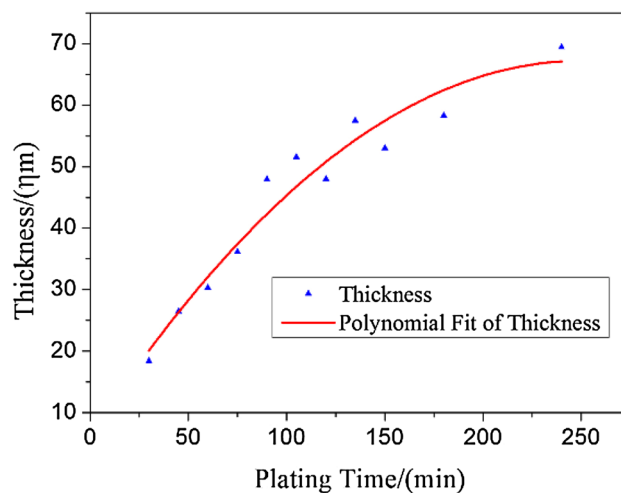

Fig. 3 Morphology of fracture after bond strength test. Inset is an enlarged image of the crack edge area

Fig. 4 Growth curve of the Ni–P coating film on diamond/Al composites as a function of plating time

The electroless-plated Ni–P film has a crystalline microstructure. Figure 5a shows the comparison of XRD patterns between the as-received composite and the coated composite. It can be determined that both the as-received diamond/Al composite and the coated diamond/Al composite are polycrystalline according to the morphologies of diffraction peaks that were observed. Before electroless deposition, the straight baseline indicated that no crystal impurities were present in the diamond/Al composite. However, some wide and weak intensity peaks were observed in the coated composite after electroless deposition. Figure 5b clearly shows the XRD pattern of Ni–P coating and the peaks of Ni oriented along the {111}, {200}, and {220} planes. However, no obvious peaks of phosphorous or possibly existing phosphorus compounds were observed in the pattern, which should considered to be a result of the extremely weak intensity peaks of phosphorus or phosphorus compounds.

3.2 Interfacial reaction within SAC305 and Sn63Pb37 solder joints

After soldering the Ni–P coated diamond/Al composites with Cu dummy chips, the representative lead-free and tin–lead die-attach soldering structures were obtained. The IMCs formed at the interface between the coating layer and solder alloy were characterized in detail, which greatly impacted the reliability of the solder joint as well as the interfacial shear strength. The cross-sectional images of SAC305 and Sn63Pb37 solder joints are shown in Fig. 6a and b, respectively, in which the interface at the composite side is shown to be much rougher than that at the chip side. Figure 6c shows an enlarged interfacial image between the SAC305 solder and the Ni–P coating layer. Scallop-shaped $(Cu,Ni)_6Sn_5$ existed at the interface, and its thickness varied largely from position to position. Block-shaped $(Cu,Ni)_6Sn_5$

was also found inside the solder and was distributed randomly due to spalling. There were a mass of Ag_3Sn particles as well inside the SAC 305 solder, which had a reticular structure. Figure 6d presents the interfacial microstructure of the Sn63Pb37 solder joint at the composite side. Scallop-shaped $(Cu,Ni)_6Sn_5$ was also observed at the interface. Some $(Cu,Ni)_6Sn_5$ blocks grew to be extremely larger than others and were segregated from the interface into the solder. Although $(Cu,Ni)_6Sn_5$ compounds can also be formed within the solder alloy during soldering, their sizes are small due to the limited concentration of Cu in the solder matrix. However, the $(Cu,Ni)_6Sn_5$ compounds formed in the interfacial reaction are big and will segregate into the solder matrix due to the spalling mechanism. Moreover, a Pb-rich phase was observed in the Sn63Pb37 solder alloy.

Comparing the detailed interfacial microstructures at the composite side, some differences between the two solder joints can be found. First, the average thickness of IMC in the SAC305 solder joint was higher than that in the Sn63Pb37 solder joint. Second, the $(Cu,Ni)_6Sn_5$ compound at the interface of SAC305/Ni–P had a larger size than that in the Sn63Pb37 solder joint. This was because the soldering/reflowing temperature of SAC305 was higher than that of Sn63Pb37 due to a higher melting point of lead-free solder alloy, which can contribute to the IMC growth. However, no Kirkendall voids or cracks were found at the interface of both two solder joints, which illustrates the outstanding solderability and reliability of the Ni–P coating layer on the diamond/Al composite.

The standard shear test was conducted on these two die-attach structures, as illustrated in Fig. 1b, and the results were shown in Fig. 7. The shear strengths of the SAC305/coating and the Sn63Pb37/coating were in a similar range. The average strength of the SAC305 soldering structure was 39.9 MPa, whereas that of the Sn63Pb37
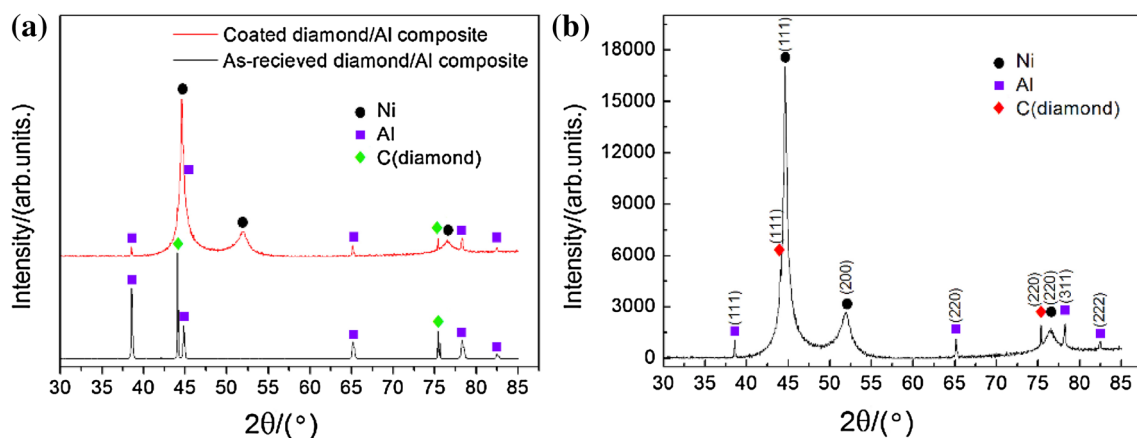

Fig. 5 **a** XRD patterns of as-received diamond/Al composite and Ni–P coated diamond/Al composite, **b** detailed XRD pattern of Ni–P coated diamond/Al composite. (Color figure online)
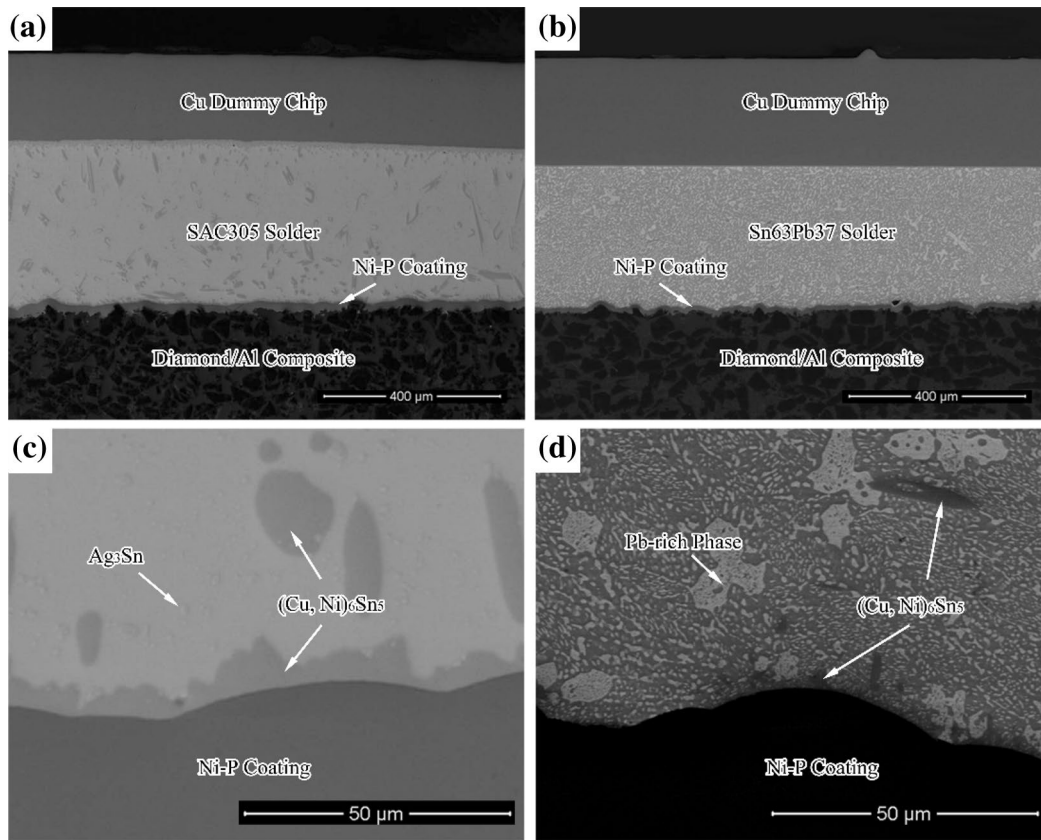
Fig. 6 Cross-sectional views of **a** SAC305 and **b** Sn63Pb37 solder joints as well as the microstructure of **c** SAC305 and **d** Sn63Pb37 soldering interfaces
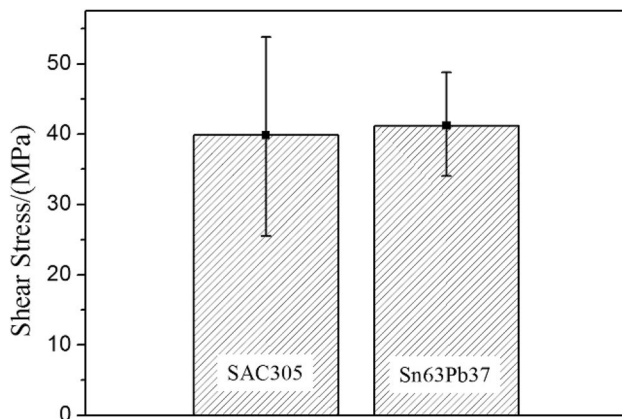

Fig. 7 Shear strength of SAC305 and Sn63Pb37 soldering structures

was 41.2 MPa. The variation range of shear strengths for the Sn63Pb37/coating structure appeared to be smaller, which indicated a steady performance of the Sn63Pb37 solder alloy. However, all the minimum shear strengths of both solder joints met the requirements for electronic industrial applications (MIL-STD-883G, thereby enabling those to withstand a minimum force of 5 kg when the die

area is larger than $64 \times 10^{-4} (\text{IN})^2$, which is equivalent to a maximum strength of 12.1 MPa).

3.3 Growth kinetics of (Cu,Ni)6Sn5 compound during thermal storage

Figure 8 shows the changes of IMCs at the interface of SAC305/Ni–P coating after different thermal storages. At 125 and 150 °C, the thickness of $(\text{Cu,Ni})_6\text{Sn}_5$ was raised slightly with an increase in storage time. While at 175 °C, the thickness of $(\text{Cu,Ni})_6\text{Sn}_5$ grew fast during the thermal storage process. Within the solder alloy, Ag_3Sn gradually turned from the organized reticular structure into randomly distributed particles as the storage time increased. For the Sn63Pb37/coating interface, as shown in Fig. 9, a similar growth trend of $(\text{Cu,Ni})_6\text{Sn}_5$ can be observed. The thickness of the $(\text{Cu,Ni})_6\text{Sn}_5$ in Sn63Pb37 soldering structure had a dramatic increase at 175 °C, but the morphology of the Pb-rich phase changed little even at different temperatures.

As reported by Shang et al. [27], the relationship between the thickness of the IMC formed during thermal storage and the storage time can be expressed by the following formula:
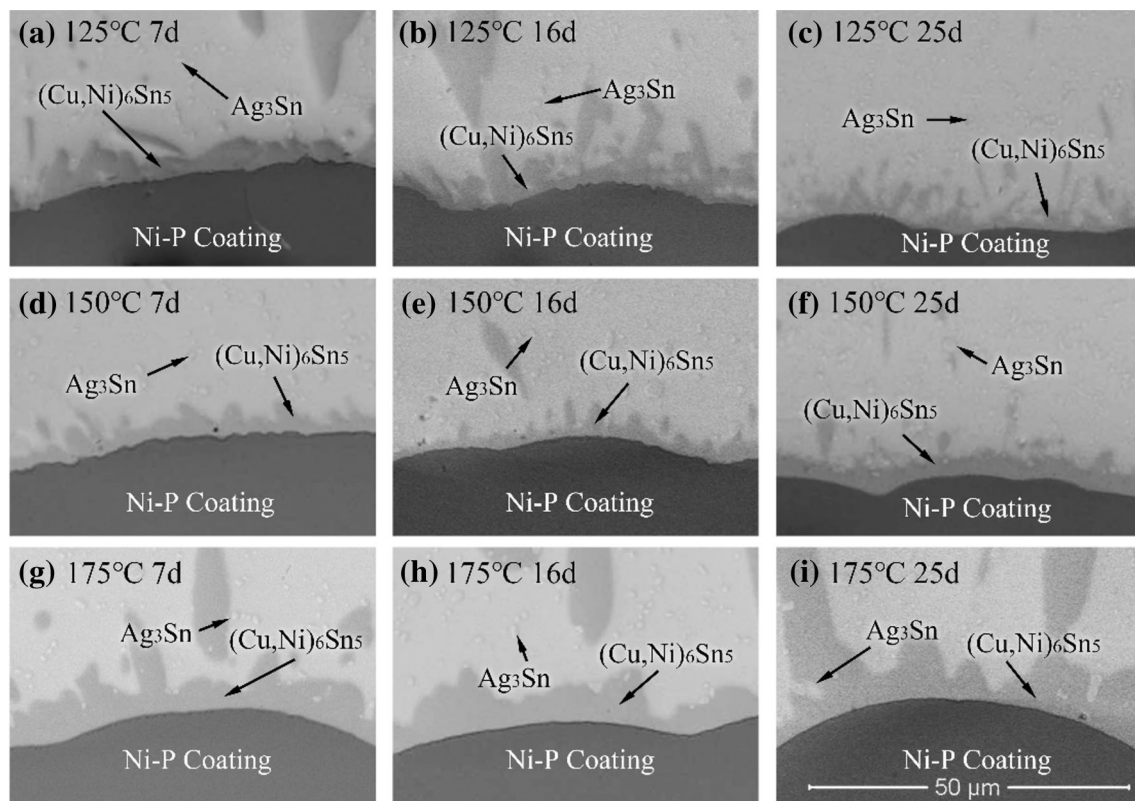
$$d - d0 = Dt^n \tag{5}$$

Fig. 8 Microstructural evolution of intermetallic compounds at the interface of SAC305/Ni–P during high temperature storage at different temperatures for different days

where t is the thermal storage time, d is the thickness of IMC at time t, d_0 is the thickness of IMC before thermal storage, D is the IMC growth rate coefficient, which is approximate to IMC diffusion coefficient when the interfacial reaction is controlled by diffusion, and n is the time index. When n=0.5, the IMC growth depends on diffusion. When n=1, the IMC growth depends on a chemical reaction.

The statistical thickness of interfacial IMC after storage at different temperatures for different storage times were measured systematically to analyze the relationship between the IMC thickness and the square root of the storage time at different storage temperatures. For both the SAC305 and Sn63Pb37 solder joints, the relationship is approximately linear, as shown in Fig. 10, which demonstrates that the IMC growth is controlled by elemental diffusion in this work.

As the main species of interfacial IMC in both the SAC305 and Sn63Pb37 solder joints is $(Cu,Ni)_6Sn_5$, its diffusion coefficient can be calculated as follows according to the Arrhenius formula, which provides the relationship between the diffusion coefficient and the diffusion activation energy [28]:

$$D = D_0 \exp(-Q/RT) \tag{6}$$

where D is the diffusion coefficient, D_0 is the diffusion constant, Q is the diffusion activation energy, T is the temperature, and R is the gas constant. The calculated results are shown in Table 2. Compared with the diffusion coefficients of Cu_6Sn_5, as reported by Li et al. [29] (4.54×10^{-17} m/s² at 160 °C in SAC305/Cu, 49.9 kJ/mol) and Wu et al. [30] (8.23×10^{-18} m/s² at 150 °C in Sn63Pb37/Cu, 76.92 kJ/mol), the diffusion coefficients of $(Cu,Ni)_6Sn_5$ that are formed on Ni–P coating layer are smaller. It indicates that the participation of Ni element in the interfacial reaction between Cu and Sn can inhibit the IMC growth due to the smaller diffusion coefficient. This is another merit of Ni–P coating as a metallization layer on the diamond/Al composite. Again, no cracks or voids were observed at the interfaces of both solder joints. Even the storage temperature was kept at 175 °C for 25 days. The above phenomena demonstrate the good reliability of Ni–P coating at high temperatures.

4 Conclusion

1. The coating of the diamond/Al composite is essential for its application in microelectronic device packaging, which has never been reported before. With the modified
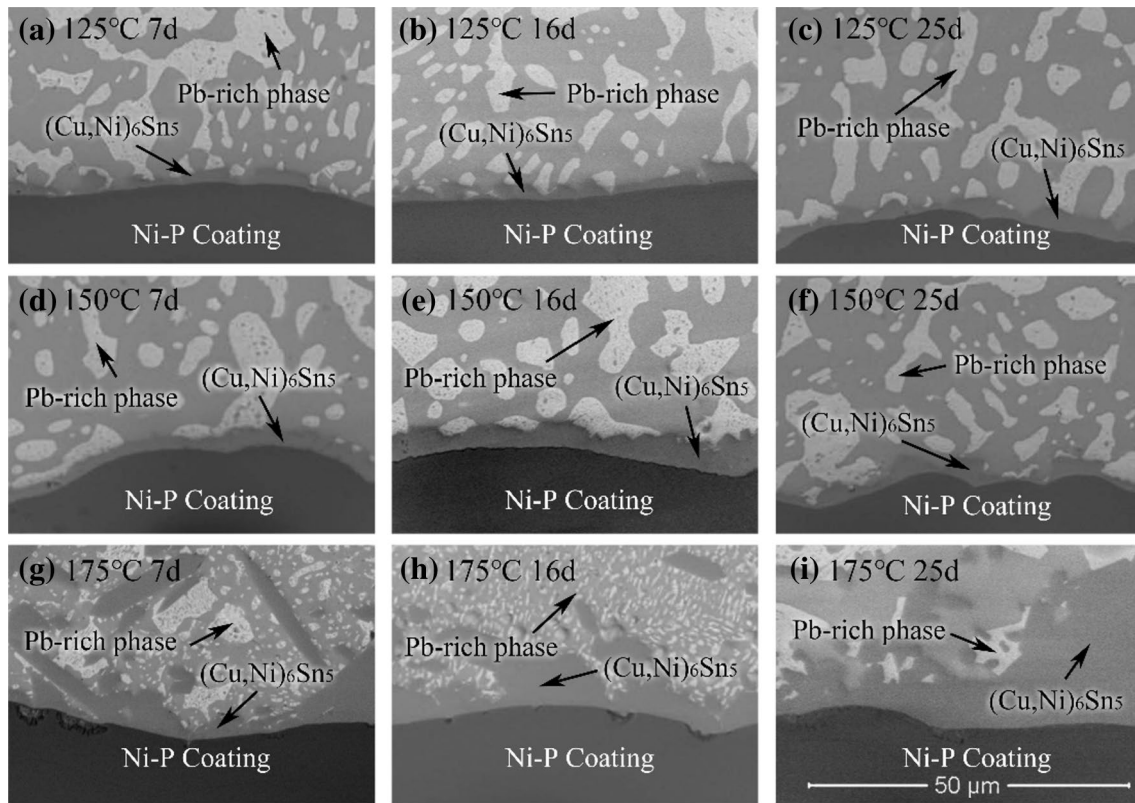
Fig. 9 Microstructural evolution of intermetallic compounds at the interface of Sn63Pb27/Ni–P during high temperature storage at different temperatures for different days
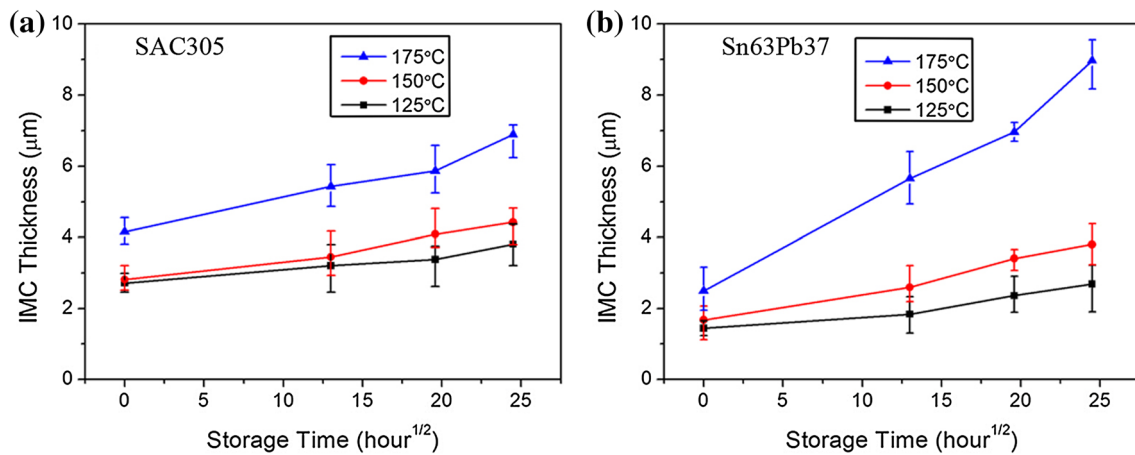

Fig. 10 Relationship between square root of storage time and (Cu,Ni)6Sn5 thickness in **a** SAC305 and **b** Sn63Pb37 soldering structures

Table 2 Diffusion coefficient of $(Cu,Ni)_6Sn_5$ in SAC305 and Sn63Pb37 soldering structures

Soldering structure	$D_{125°C}$ (m/s^2)	$D_{150°C}$ (m/s^2)	$D_{175°C}$ (m/s^2)	Q (kJ/mol)
SAC305	4.17101E−19	1.18556E−18	3.45216E−18	62.6
Sn63Pb37	6.11003E−19	2.15111E−18	1.67827E−17	97.7

recipe of the electroless plating bath and the adjusted electroless plating process, we successfully fabricated a crystalline Ni–P coating film on the diamond/Al composite surface for the first time. The coating film was glossy and smooth and covered the surface totally with a bonding strength of 15.1 MPa. The relationship between plating time and coating thickness appeared to be nearly linear within 120 min at a growth rate of about 0.42μ m/min.

2. For the non-wettable diamond/Al composite surface, the Ni–P coating can improve the solderability of the composite immensely. After soldering with the Cu dummy chip, no cracks and voids were observed at the interfaces between the Ni–P film and the SAC305/Sn63Pb37 solders. The shear strengths of both the SAC305 (39.9 Mpa) and Sn63Pb37 (41.2 Mpa) solder joints are satisfied with respect to the standards in the electronic industry, which demonstrates the excellent reliability of the Ni–P coating.

3. According to the results of the thermal storage experiments that were conducted at 125, 150, and 175 °C, the growth of the $(Cu,Ni)_6Sn_5$ compound was driven by elemental diffusion. The diffusion coefficients of $(Cu,Ni)_6Sn_5$ at the different storage temperatures were calculated, which was 3.45×10^{-18} m/s^2 for SAC305 and 1.68×10^{-17} m/s^2 for Sn63Pb37 at 175 °C. The diffusion activation energy of $(Cu,Ni)_6Sn_5$ at the interface of the SAC305 and Sn63Pb37 solder joints was determined as 62.6 and 97.7 kJ/mol, respectively. All these values are remarkably lower than those reported in literatures, which demonstrates a slow IMC growth on the Ni–P coating and ensures the outstanding reliability of the soldering structures.

References

1. H.E. Ahmed, B.H. Salman, A.S. Kherbeet, M.I. Ahmed, Int. J. Heat Mass Transf. **118**, 129 (2018)
2. S.K. Sahoo, M.K. Das, P. Rath, Renew. Sustain. Energy Rev. **59**, 550 (2016)
3. C. Zhang, R.C. Wang, Z.Y. Cai, C.Q. Peng, N.G. Wang, J. Mater. Sci. Mater. Electron. **26**, 185 (2015)
4. K. Hanada, K. Matsuzaki, T. Sano, J. Mater. Process. Technol. **154**, 514 (2004)
5. K. Mizuuchi, K. Inoue, Y. Agari, Microelectron. Reliab. **79**, 5 (2017)
6. I.E. Monje, E. Louis, J.M. Molina, Composites A **A67**, 70 (2014)
7. H.Y. Zhou, Y.L. Yin, Z.L. Shi, C.J. Wu, J.Y. Liu, J. Mater. Sci.: Mater. Electron. **28**, 721 (2017)
8. C.X. Li, X.T. Wang, L.H. Wang, J.W. Li, H.X. Li, H.L. Zhang, Mater. Des. **92**, 643 (2016)
9. C. Zhang, Z.Y. Cai, R.C. Wang, C.Q. Peng, Y. Feng, Surf. Coat. Technol. **313**, 347 (2017)
10. Z.Y. Xiu, X. Wang, M. Hussain, C. Feng, L.T. Jiang, Trans. Nonferr. Met. Soc. China. **23**, 3584 (2013)
11. S.D. Ma, N.Q. Zhao, C.S. Shi, E.Z. Liu, C.N. He, F. He, L.Y. Ma, Appl. Sur. Sci. **402**, 372 (2017)
12. C. Xue, J.K. Yu, Surf. Coat. Technol. **217**, 46 (2013)
13. X.Y. Liu, W.G. Wang, D. Wang, D.R. Ni, L.Q. Chen, Z.Y. Ma, Mater. Chem. Phys. **182**, 256 (2016)
14. Y. Zhang, J.W. Li, L.L. Zhao, H.L. Zhang, X.T. Wang, Mater. Des. **63**, 838 (2014)
15. H. Zhang, Q.S. Zhu, Z.Q. Liu, L. Zhang, H.Y. Guo, C.M. Lai, J. Mater. Sci. Technol. **30**, 928 (2014)
16. L.Y. Gao, H. Zhang, C.F. Li, J.D. Guo, Z.Q. Liu, J. Mater. Sci. Technol. (2018). https://doi.org/10.1016/j.jmst.2017.11.046
17. L.Y. Gao, C.F. Li, P. Wan, Z.Q. Liu, J. Mater. Sci.: Mater. Electron. **28**, 1 (2017)
18. H. Zhang, D. Wu, L. Zhang, Z.Z. Duan, C.M. Lai, Z.Q. Liu, Acta Metall. Sin. **48**, 1273 (2012)
19. L.Y. Gao, Z.Q. Liu, C.F. Li, J. Electron. Mater. **46**, 5338 (2017)
20. X.B. Xi, H. Miao, R.H. Zhang, J.L. Cheng, Surf. Coat. Technol. **297**, 27 (2016)
21. D.G. Liu, Y.J. Mai, J. Sun, Z.J. Luan, W.C. Shi, L.M. Luo, H. Li, Y.C. Wu, Ceram. Int. **43**, 13133 (2017)
22. T. Yuan, C.C. Jia, H. Guo, J. Univ. Sci. Technol. B **34**, 926 (2012)
23. C. Xu, C.C. Jia, H. Guo, Z.H. Bai, M. Li, J. Univ. Sci. Technol. B. **35**, 1500 (2013)
24. X.Y. Liu, W.G. Wang, D. Wang, B.L. Xiao, D.R. Ni, L.Q. Chen, Z.Y. Ma, Acta Metall. Sin. **53**, 869 (2017)
25. Y.H. Dong, X.B. He, R. Ud-Din, C.Y. Guo, X. Liang, Y.T. Huang, X.H. Qu, Int. J. Min. Met. Mater. **18**, 479 (2011)
26. Z. Sharifalhoseini, M.H. Entezari, Appl. Surf. Sci. **351**, 1060 (2015)
27. P.J. Shang, Z.Q. Liu, X.Y. Pang et al., Acta Mater. **57**, 4697 (2009)
28. S. Kumar, C.A. Handwerker, M.A. Dayananda, J. Phase Equilib. Diffus. **32**, 309 (2011)
29. S. Li, Y.F. Yan, Y.M. Zhao, Y.Y. Xu, Trans. Met. Heat Treat. **35** 24 (2014)
30. Y.J. Wu, J.A. Sees, C. Pouraghabagher, L.A. Foster, J.L. Marshall, E.G. Jacobs, R.F. Pinizzotto, J. Electron. Mater. **22**, 769 (1993)